REPORT NO.
UCB/SEMM-2000/06

STRUCTURAL ENGINEERING
MECHANICS AND MATERIALS

A MULTI-VARIANT MARTENSITIC PHASE TRANSFORMATION MODEL: FORMULATION AND NUMERICAL IMPLEMENTATION

BY

SANJAY GOVINDJEE

AND

CHRISTIAN MIEHE

JUNE 2000

DEPARTMENT OF CIVIL AND ENVIRONMENTAL ENGINEERING
UNIVERSITY OF CALIFORNIA
BERKELEY, CALIFORNIA

A Multi-Variant Martensitic Phase Transformation Model: Formulation and Numerical Implementation

Sanjay Govindjee *
Christian Miehe †

June 26, 2000

Abstract

The development of models for shape memory alloys and other materials that under-go martensitic phase transformations has been moving towards a common generalized thermodynamic framework. Several promising models utilizing single martensitic variants and some with multiple variants have appeared recently. In this work we develop a model in a general multivariant framework that is based upon lattice correspondence variants and the use of dissipation arguments for the generation of specialized evolution equations. The evolution equations that appear are of a unique nature in that not only are the thermodynamic forces restricted in range but so are their kinematic conjugates. This unusual situation complicates the discrete time integration of the evolution equations. We show that the trial elastic state method that is popular in metal plasticity is inadequate in the present situation and needs to be replaced by a nonlinear programming problem with a simple geometric interpretation. The developed integration methodology is robust and leads to symmetric tangent moduli. Example computations show the behaviour of the model in the pseudoelastic

*Associate Professor of Civil Engineering, University of California Berkeley, govindjee@ce.berkeley.edu

†Professor of Civil Engineering, Institüt für Mechanik (Bauwesen), Universität Stuttgart, cm@mechbau.uni-stuttgart.de

range. Of particular interest is the fact that the model can predict the generation of habit plane-like variants solely from the lattice correspondence variants; this is demonstrated through a comparison to the experimental work of Shield [35].

Contents

1 Introduction **4**
- 1.1 Modeling Overview 4
- 1.2 Model Time Integration 4
- 1.3 Goals and Characteristics of the Proposed Model 6
- 1.4 Outline 7

2 Model Equations **8**
- 2.1 Free Energy 8
- 2.2 Stress Response and Generalized Thermodynamic Forces . . . 12
- 2.3 Transformation Inequality 12
- 2.4 Maximum Dissipation Hypothesis 13
- 2.5 Rate Equations 15
- 2.6 Discussion 16

3 Time Integration **17**
- 3.1 Backward Euler 18
- 3.2 Active Set Solution Strategy 19
- 3.3 Determination of an Elastic Time-step 19
- 3.4 Evolution: 23
- 3.5 Global Tangent Operator 24

4 Examples **25**
- 4.1 Stress Strain Response 27
- 4.2 Phase fraction histories 27
- 4.3 Global Convergence Behavior 33

5 Closure **33**

A Algorithms for d_1 and d_2 **38**
- A.1 d_1 2-norm 38
- A.2 d_2 2-norm 41

B Overall algorithmic details **41**

List of Tables

1 Summary of Time Continuous Constitutive Equations 14
2 Summary of Discrete Equations to be solved at t_{n+1} 18
3 Material Properties for Simulations 27
4 Global Residual Norms 33

List of Figures

1 Polytope $\mathbb{P}^{n-1}$ 11
2 Elastic conjugate force domain 17
3 Optimization Geometry 2 constraints 21
4 Optimization Geometry 1 constraint 22
5 Simulation Geometry and Boundary Conditions 26
6 Stress Strain Response 28
7 Spatial Austenite Distribution 29
8 Phase fraction history A1-T1b 30
9 Phase fraction history A1-T2b 31
10 Phase fraction history A1-T3b 32

1 Introduction

Alloys that undergo martensitic phase transformations provide a unique medium from which to design a variety of novel engineering devices. In particular, the class of alloys that are known as shape memory alloys possess unique features that make them attractive in applications ranging from simple eyeglass frames all the way to jet engine components and advanced medical prosthetics; see for example Duering, Melton, Stockel, and Wayman [16] or Funakubo [17]. There are two basic effects that are exploited in the use of such alloys: (1) is the production and consumption of martensites under the application of stress and (2) the production or consumption of martensite during the cooling or respectively heating of the alloy. What makes these alloys even more interesting is the fact that both of these effects are reversible through the application of an appropriate stress and temperature excursion.

1.1 Modeling Overview

We are interested, in this work, in the macroscopic modeling in multi-dimensions of materials with an evolving martensitic structure. We are not interested in fine details of the microstructure but rather gross measures of it, its evolution, and its affect on the macroscopic stress strain behavior of such materials. The governing free energy and evolution equations of such a model have been presented in part in several works; see for example Boyd and Lagoudas [12, 13], Siredey, Patoor, Berveiller, and Eberhardt [39], Bo and Lagoudas [11], Idesman, Levitas, and Stein [26], Levitas, Idesman, and Stein [28], Sun and Hwang [41], and Huang and Brinson [25] where aspects of continuum thermodynamics, often in conjunction with Eshelby arguments, are utilized to generate a model. Alternatively, see Abeyratane and Kim [2], Abeyaratne, Kim, and Knowles [1], Achenbach [3], Achenbach, Atanackovic, and Müller [4], Achenbach and Müller [5], Müller and Xu [33], Govindjee and Hall [20, 19], and Hall and Govindjee [23] where methods of statistical physics are applied to generate a suitable evolutionary model structure.

1.2 Model Time Integration

The time integration of such constitutive models has not received as much attention as their modeling. By time integration we mean the integration of the constitutive equations in time under, say, strain and temperature control

as would be common in a FEM code. There are two primary difficulties in time integrating models of the type referenced above. One is that the internal variables are constrained to lie in a convex polytope. This restriction is a consequence of mass conservation and comes into play numerically at the completion of a transformation process. The second is associated with the selection of what type of transformation if any is actually taking place during a discrete time step during the integration process; this is a branch selection (uniqueness) issue.

Time integration work has been done on models of the Tanka [42] type by Brinson and Lammering [14]; see also Govindjee and Kasper [21]. These models are, however, in general essentially only one-dimensional models and their extension to multi-dimensions is somewhat unclear; for one such extension see Lubliner and Auricchio [29]. Further, they suffer from a branch switching pathology that does not have a clear solution [21]. In the context of multi-dimension models, the recent work of Qidwai and Lagoudas [34] examines a model that is formally similar in mathematical structure to classical plasticity. They apply both the return map and the convex cutting plane algorithm to a shape memory alloy model with a single martensite variant. The model that is presented, while multi-dimensional, is essentially restricted to proportional loading due to certain assumptions on the character of the transformation strain. It is not clear if the numerical model suffers from the branch selection problem but it is noted that the numerical procedure is based on a trial stress approach which has been shown in 1-D for Tanaka type models to *not* fully characterize the branch; see Govindjee and Kasper [21]. It is also noted that while the authors propose methods to deal with transformation completion, the techniques are introduced in an *ad hoc* fashion since the time continuous equations do not explicitly account for the polytope constraint. In Hall and Govindjee [23] a multi-dimensional model that includes the polytope constraint and its computational realization is presented. This model is based on notions from statistical physics and involves the direct integration of a Markov process. While [23] presents a model that is anisotropic and valid for non-proportional loading it lacks in its structure the explicit notion of an interaction energy between martensite and austenite variants and is thus only qualitative. The computational technique is based upon unconstrained integration and a polytope projection algorithm to deal with the mass conservation issue. The model does not suffer from branch selection problems due to its Markov structure. Unfortunately, the numerical methods proposed depend crucially on the Markov structure of the rate

equations and are not generalizable to other model types. In Siredey et.al. [39] a model is proposed that explicitly accounts for the polytope constraint in the time continuous equations. Huang and Brinson [25] have used this model structure and briefly present an integration method in an appendix that relies on penalty methods to effect the integration of the model. The geometric setting of the model and its numerical approximation are, however, not explored in detail.

1.3 Goals and Characteristics of the Proposed Model

The goals of this paper are multi-fold but generally revolve about the issues of the creation and numerical approximation of an evolutionary martensitic model. As with the literature cited above we will introduce a continuum model that is based on internal variables – the phase fractions. In particular, we will consider a model that is based only upon lattice correspondence variants since these are the fundamental transforming units in the material systems of interests. The introduction of habit plane variants (see for example Siredey et.al. [39] or Gao, Huang, and Brinson [18]) is avoided as we feel a well posed model should automatically generate such structures through "natural" evolution under appropriate loading conditions. Further a model based on lattice correspondence variants also possess the ability to handle complex phenomena such as detwinning and reorientation transformations. Lastly, a model based on lattice correspondence variants avoids the difficulties associated with enumerating all the possible habit plane solutions. This can be a particularly difficult problem for materials with low symmetry martensites. For example, in Ni-Ti alloys there are 12 monoclinic lattice correspondence variants (martensites) but the number of habit plane variants is (at least) 192; see Hane and Shield [24].

Like, Siredey et.al. [39] and Huang and Brinson [25] we will develop our model equations by appealing to methods of continuum thermodynamics. In particular we will borrow their notion of the replacement of the free energy density of the material with a Lagrangian potential that explicitly accounts for the mass conservation constraints on the internal variables (phase fractions) in the model. In extension of these previous works, we formalize a number of model development details and elaborate upon the geometric setting of the model equations in an effort to aide in understanding their continuum structure as well as in exploiting the geometry for numerical approximation purposes. Note that the discussion will take place in the setting

of a relatively arbitrary criteria for the phase transformation as opposed to a reliance upon the infinity norm as been previously considered by these authors.

The concrete form of the free energy function that we base the model upon is from the work of Govindjee and Mielke [22]. These authors develop a free energy structure from the view point of quasi-convexity; a notion which amounts to the minimum known mathematical structure required for existence of solutions to such models. In particular they consider the n-variant problem within a context appropriate for an evolutionary model. In the present work we will utilize an estimate to the structure that emanates from the quasi-convexity arguments to develop our evolutionary model. Note that these developments are similar to those contained in the works of Kohn [27] and Smyshlyaev and Willis [40] where attention is focused on an equilibrium problem for two and three variants, respectively – not on an evolutionary system.

Our numerical approach will be based as in classical plasticity upon a trial state methodology. In contrast to the work of Qidwai and Lagoudas [34], we will not use the trial stress, for reasons mentioned above, but rather we will utilize a trial conjugate driving force method. The conjugate driving force being referred to here will be the thermodynamic conjugate to the internal variables. Of special interest is the geometric setting of this trial state and how one can determine from it when phase transformation will take place and when it will not. It will be shown that the trial state procedure in the space of conjugate forces in conjunction with a simple nonlinear programming problem can be used to detect transformation steps from elastic steps. For ease of discussion and presentation, we will primarily consider the case of a C^1 transformation criteria. It is noted, however, that the methods presented are also equally valid for the case of non-differential transformation surfaces when one introduces the notion of a sub-differential.

1.4 Outline

The outline of the paper is as follows. We first define the time continuous equations that define our phase transformation model. This includes the presentation of our free energy function and its associated Lagrangian, the stress strain relations and the definitions of the generalized thermodynamic forces, the transformation criteria, and phase transformation evolution law. This is followed by a discussion of the rate equations and the geometry associated

with the time evolution of the model. Next, we apply a finite difference method to integrate the time continuous equations and discuss in detail the geometry of the solution of these discrete equations. We then apply the model in a finite element simulation of the extension and unloading of a rectangular tension specimen with a non-homogeneous deformation state. The results of the computation are compared to experimental data and good agreement is seen with respect to overall response as well as to microstructural response measures. The paper closes with a brief discussion of the presented material and issues that remain outstanding.

2 Model Equations

In this section we develop the time continuous equations for our model. We begin by first stating the free energy structure of our material. This is followed by the replacement of our free energy with a Lagrangian potential that accounts for certain kinematic constraints of the material. This leads us to the expression for the stresses and the generalized thermodynamic forces associated with the phase transformation. Utilizing a postulated transformation criteria we are then able to close our system of constitutive equations with an evolution law for the internal variables of the model that represent the phase fractions of the variants. This evolution law emanates from an assumption of maximum dissipation and gives rise to a symmetric structure to the rate equations. The geometric setting of the model is also discussed with a view towards its exploitation in the development of numerical algorithms.

2.1 Free Energy

Our goal is to describe the evolution of a martensitic phase transformation within an internal variable formulation. Our point of departure is the free energy function of Govindjee and Mielke [22]

$$\Psi(\boldsymbol{\varepsilon}, \boldsymbol{\xi}) = \boldsymbol{\xi} \cdot \boldsymbol{\psi}(\boldsymbol{\varepsilon}) + \Psi^M(\boldsymbol{\xi}), \tag{1}$$

where $\boldsymbol{\xi} \in \mathbb{R}^n$ is the vector of phase fractions and is understood as the internal variable of the formulation. The decoupling present in Eq. (1) arises naturally from the quasi-convexification formalism employed in its development and is intimately connected to the notion of homogenization of optimal

microstructures; see Govindjee and Mielke [22] for additional details and references. Above, n is the number of martensitic variants plus one for the austenite variant, Ψ^M is the free energy of mixing which is convex and non-positive, $\boldsymbol{\varepsilon} \in \mathbb{S}^d$ is the symmetric small strain tensor for a d-dimensional problem ($d \in \{1, 2, 3\}$), and $\boldsymbol{\psi} \in \mathbb{R}^n$ is defined in the standard orthonormal basis in terms of the components

$$\psi^\alpha = \frac{1}{2}(\boldsymbol{\varepsilon} - \boldsymbol{\varepsilon}^\alpha) : \mathbb{C} : (\boldsymbol{\varepsilon} - \boldsymbol{\varepsilon}^\alpha) + M^\alpha. \tag{2}$$

Throughout the paper, we utilize a single dot ($\cdot$) to denote the standard inner product for vectors in $\mathbb{R}^n$ and the double dot ($:$) to denote double contraction between rank-2 tensors and between a rank-2 tensor and a rank-4 tensor in $\mathbb{R}^d$. The superscript greek letters are indices that range from 1 to n the number of crystallographic variants in the problem. For simplicity we assume each martensite and austenite is governed by the same rank-4 *isotropic* elasticity tensor $\mathbb{C}$. $\boldsymbol{\varepsilon}^\alpha$ is the generalized transformation strain for the α variant and M^α is the minimum free energy value at each variant. The explicit expressions for the generalized transformation strain is

$$\boldsymbol{\varepsilon}^\alpha = \boldsymbol{\varepsilon}^{\alpha_t} + \Delta\theta\boldsymbol{\varepsilon}^{\alpha_\theta}\,, \tag{3}$$

where $\Delta\theta = \theta - \theta_o$ is the temperature difference from a reference absolute temperature θ_o, $\boldsymbol{\varepsilon}^{\alpha_\theta}$ is the thermal coefficient of expansion tensor for variant α, and $\boldsymbol{\varepsilon}^{\alpha_t}$ is the stress free martensitic transformation strain for variant α with reference to a zero strain austenite. The minimum of each potential is given by Abeyratane and Kim [2] and Abeyaratne, Kim, and Knowles [1] as

$$M^\alpha = \rho c(1 - \log(\theta/\theta_o)) - \rho l^\alpha(1 - \theta/\theta_o) - \frac{1}{2}\Delta\theta^2\boldsymbol{\varepsilon}^{\alpha_\theta} : \mathbb{C} : \boldsymbol{\varepsilon}^{\alpha_\theta}\,, \tag{4}$$

where ρ is the mass density of the material, c is a heat capacity, and l^α is the latent heat of transformation for each variant. For simplicity we assume all the variants share the same mass density and heat capacity. Eq. (4) was designed to take into account the relative motion of the free energy minima of the variants with respect to temperature.

The expression for the free energy of mixing can be developed in a number of different ways. Following along the lines of Kohn [27] for the two variant problem and Smyshlyaev and Willis [40] for the three variant problem, Govindjee and Mielke [22] have utilized the quasi-convexification method to

determine an expression for the mixing energy for the general n-variant problem. The form for this expression is posed as an optimization problem with respect to H-measures of the material microstructure and in the n-variant case can not be given in closed form. However, good bounds can be determined for it as shown in Govindjee and Mielke [22]. In the examples section of the paper, we will use a Reuß–like lower bound

$$\Psi^M(\boldsymbol{\xi}) \geq \Psi^M_{\text{Reuß}}(\boldsymbol{\xi})\,, \tag{5}$$

which for many values of the phase fractions is actually the exact solution to the H-measure optimization problem; for more details on H-measures see Tartar [43]. The explicit form of the Reuß bound is given as

$$\Psi^M_{\text{Reuß}}(\boldsymbol{\xi}) = -\frac{1}{2}\sum_{\alpha=1}^{n} \xi^\alpha \boldsymbol{\varepsilon}^\alpha : \mathbb{C} : \boldsymbol{\varepsilon}^\alpha + \frac{1}{2}\sum_{\alpha=1}^{n}\sum_{\beta=1}^{n} \xi^\alpha \xi^\beta \boldsymbol{\varepsilon}^\alpha : \mathbb{C} : \boldsymbol{\varepsilon}^\beta. \tag{6}$$

There are a variety of different means to derive Eq. (6). Perhaps the most transparent derivation comes by first constructing a Gibbs mixture potential and then taking its Legendre transformation. The needed Gibbs energy is given by

$$G(\boldsymbol{\sigma}, \boldsymbol{\xi}) = \boldsymbol{\xi} \cdot \boldsymbol{g}\,, \tag{7}$$

where the components of $\boldsymbol{g}$ are $g^\alpha = -\frac{1}{2}\boldsymbol{\sigma} : \mathbb{C}^{-1} : \boldsymbol{\sigma} - \boldsymbol{\sigma} : \boldsymbol{\varepsilon}^\alpha$ and $\boldsymbol{\sigma}$ is the stress tensor. The Legendre transformation of Eq. (7) gives

$$\sup_{\boldsymbol{\sigma}} \{\boldsymbol{\xi} \cdot \boldsymbol{g} + \boldsymbol{\sigma} : \boldsymbol{\varepsilon}\} = \boldsymbol{\xi} \cdot \boldsymbol{\psi} + \Psi^M_{\text{Reuß}}(\boldsymbol{\xi})\,. \tag{8}$$

Thus we see that $\Psi^M_{\text{Reuß}}(\boldsymbol{\xi})$ simply embodies the notion that there is no mixing energy in the "stress-ensemble" picture.

The kinematic internal variable $\boldsymbol{\xi}$ is restricted by the principle of mass conservation to satisfy the following two constraints

$$\begin{aligned} \boldsymbol{e}^* \cdot \boldsymbol{\xi} - 1 &= 0\,, & (9)\\ -\boldsymbol{\xi} &\leq 0\,, & (10) \end{aligned}$$

where $\boldsymbol{e}^* \in \mathbb{R}^n$ is a vector whose components have value unity in the standard basis for $\mathbb{R}^n$; i.e. it serves as the trace operator for vectors in $\mathbb{R}^n$. Eq. (9) shows that the model has more internal variables than are actually necessary. This point has important implications in understanding and exploiting the

geometric setting of the proposed formulation. In fact, these conditions restrict the admissible values of $\boldsymbol{\xi}$ to live in a convex polytope, $\mathbb{P}^{n-1} \subset \mathbb{R}^n$; i.e. $\boldsymbol{\xi} \in \mathbb{P}^{n-1}$. The geometric form of $\mathbb{P}^{n-1}$ is that of a hyper-tetrahedron. For example, if $n = 3$, then $\mathbb{P}^2$ is simply the (111) plane in the positive quadrant; ie. it is a triangle as visualized in Fig. 1. The presence of these constraints suggests *the replacement of the free energy function* (1) by a Lagrangian potential as has been put forward by Siredey et.al. [39] and Huang and Brinson [25]:

$$\mathcal{L}(\boldsymbol{\varepsilon}, \boldsymbol{\xi}, \boldsymbol{\gamma}, \delta) = \Psi(\boldsymbol{\varepsilon}, \boldsymbol{\xi}) - \boldsymbol{\gamma} \cdot \boldsymbol{\xi} + \delta(\boldsymbol{e}^* \cdot \boldsymbol{\xi} - 1)\,, \tag{11}$$

where the vector of multipliers, $\boldsymbol{\gamma}$, must satisfy the Kuhn-Tucker conditions

$$\boldsymbol{\gamma} \cdot \boldsymbol{\xi} = 0 \qquad \text{and} \qquad \boldsymbol{\gamma} \geq \mathbf{0} \tag{12}$$

in order to enforce the uni-lateral constraint that the phase fractions can not be negative; δ is a multiplier that enforces the constraint that the phase fractions must sum to unity.

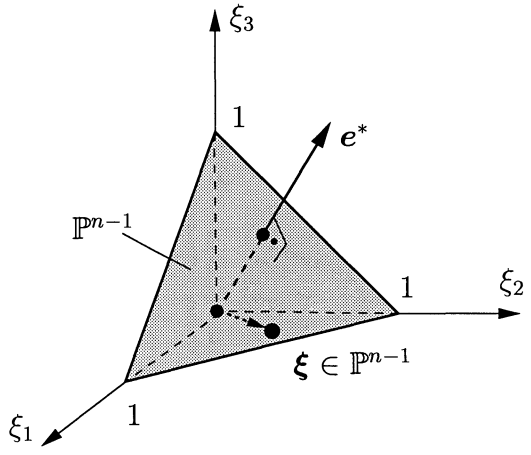

Figure 1: Constraint on internal variable. The internal variable vector $\boldsymbol{\xi}$ of phase fractions is constrained to lie in the convex polytope $\mathbb{P}^{n-1} \subset \mathbb{R}^n$. For $n = 3$, $\mathbb{P}^2 \subset \mathbb{R}^3$ is the shaded triangle shown above with orientation (normal vector) $\boldsymbol{e}^*$.

2.2 Stress Response and Generalized Thermodynamic Forces

The generalized stress-strain relation for the material can be determined by appealing to the theory of materials with internal variables and the Coleman and Noll argument [15]. This delivers after standard manipulations of the potential (11) the relation for the stress $\boldsymbol{\sigma}$ as

$$\boldsymbol{\sigma} = \partial_{\boldsymbol{\varepsilon}} \mathcal{L} = \boldsymbol{\xi} \cdot \partial_{\boldsymbol{\varepsilon}} \boldsymbol{\psi} = \sum_{\alpha=1}^{n} \xi^{\alpha} \boldsymbol{\sigma}^{\alpha} \,, \tag{13}$$

where $\boldsymbol{\sigma}^{\alpha} = \mathbb{C} : (\boldsymbol{\varepsilon} - \boldsymbol{\varepsilon}^{\alpha})$ and the relation for the thermodynamic conjugate forces to the phase fractions as:

$$\boldsymbol{f} = -\partial_{\boldsymbol{\xi}} \mathcal{L} = -\boldsymbol{\psi} - \partial_{\boldsymbol{\xi}} \Psi^{M} + \boldsymbol{\gamma} - \delta \boldsymbol{e}^{*}. \tag{14}$$

This well-established argument also leads to the dissipation inequality

$$\mathcal{D} = \boldsymbol{f} \cdot \dot{\boldsymbol{\xi}} \geq 0 \,. \tag{15}$$

What remains is to set up an evolution criteria and evolution equation for the internal variables that satisfies Eq. (15). These two steps are accomplished next.

2.3 Transformation Inequality

With the preceding definitions in place, we now construct a condition that will determine when phase transformation can take place. In the spirit of generalized internal variable models, we require the generalized thermodynamic forces to be always bounded. We express this condition as

$$\phi = \|\boldsymbol{f}\| - f_c \leq 0 \,, \tag{16}$$

where f_c is a given constant that represents the effective critical thermodynamic force required for phase transformation to occur and $\|\cdot\|$ is any well defined norm on $\mathbb{R}^n$. Define the *elastic conjugate force domain* as

$$\mathbb{E} = \{\boldsymbol{f} \mid \phi(\boldsymbol{f}) < 0\} \,. \tag{17}$$

Implied in this nomenclature is the assumption that transformation can only take place when the norm of the conjugate force is equal to f_c. Points in the

space of conjugate thermodynamic forces that satisfy this condition, ($\phi(\boldsymbol{f}) = \mathbf{0}$), define a surface that we will call the "transformation surface"; this is the set of points $\boldsymbol{f} \in \partial\mathbb{E}$. Note that for well defined norms this surface will be convex. For $\boldsymbol{f} \in \mathbb{E}$, we assume that no transformation takes place. In the works of Boyd and Lagoudas [12] and Huang and Brinson [25], for instance, they have effectively chosen to utilize the infinity norm (though they do not express it as such). In our examples, we will show that even the 2-norm can be utilized to give reasonable results and thus the differentiability issues associated with the infinity norm can be avoided if desired.

2.4 Maximum Dissipation Hypothesis

To complete the constitutive model requires the specification of an evolution law for the phase fractions. As has also been done by Boyd and Lagoudas [12] for shape memory alloys we appeal to the maximum dissipation hypothesis in the absence of other physical information. The actual dissipation structure from a physical viewpoint is an open question. We note in passing that Hall and Govindjee [23] have looked in detail at the generation of a physically based kinetic model for martensitic phase transformations. Their resultant equations which can simulate a wide class of thermomechanical processes possess an unsymmetric tangent structure and thus would not fall within the framework of maximum dissipation. Putting aside this single point of evidence which is in contradiction to maximum dissipation, we proceed to maximize the dissipation (15) with respect to the constraint (16). The examples shown in Section 4 indicate that this is a reasonable course of action.

To begin, we consider the stationary conditions for the Lagrangian potential

$$\Pi(\boldsymbol{f}, \lambda) = -\mathcal{D} + \lambda\phi \tag{18}$$

under the Kuhn-Tucker conditions

$$\lambda \geq 0\,, \qquad \phi \leq 0\,, \qquad \text{and} \qquad \lambda\phi = 0\,. \tag{19}$$

This leads to the desired evolution equation with normality structure

$$\dot{\boldsymbol{\xi}} = \lambda\partial_{\boldsymbol{f}}\phi, \tag{20}$$

which is also seen to satisfy the dissipation inequality Eq. (15) and is visualized in Fig. 2. Note that for non-differential norms one needs to introduce

Table 1: Summary of Time Continuous Constitutive Equations

Stress – Strain	
$\boldsymbol{\sigma} = \sum_{\alpha=1}^{n} \xi^{\alpha} \mathbb{C} : (\boldsymbol{\varepsilon} - \boldsymbol{\varepsilon}^{\alpha})$	(21)
Transformation Criteria	
$\phi(\boldsymbol{f}) = \|\boldsymbol{f}\| - f_c \leq 0$	(22)
$\lambda\phi = 0$	(23)
$\lambda \geq 0$	(24)
Conjugate Force	
$\boldsymbol{f} + \boldsymbol{\psi}(\boldsymbol{\varepsilon}) - \boldsymbol{\gamma} + \partial_{\boldsymbol{\xi}} \Psi^{M}(\boldsymbol{\xi}) + \delta \boldsymbol{e}^{*} = 0$	(25)
Evolution Equation	
$\dot{\boldsymbol{\xi}} - \lambda \partial_{\boldsymbol{f}} \phi = 0$	(26)
Polytope Constraint	
$-\boldsymbol{\xi} \leq 0$	(27)
$-\boldsymbol{\gamma} \cdot \boldsymbol{\xi} = 0$	(28)
$\boldsymbol{\gamma} \geq 0$	(29)
$\boldsymbol{e}^{*} \cdot \boldsymbol{\xi} - 1 = 0$	(30)

the sub-differential to the set of admissible conjugate forces; see for example Moreau [32, 31]. The practical meaning of this is the need to introduce multiple Lagrange multipliers in Eq. (18) in a manner similar to what is done for multisurface plasticity; see for example Simo, Kennedy, and Govindjee [37].

At this stage the constitutive formulation is complete; the central equations are summarized for convenience in Table 1. We next discuss the rate structure of the model.

2.5 Rate Equations

The rate structure of the equations during a possible active evolution ($\lambda \neq 0$) of the phase fractions can be determined by enforcing the condition that the conjugate force must have norm f_c and remain at f_c during evolution; i.e.

$$\dot{\phi} = \partial_{\boldsymbol{f}} \phi \cdot \dot{\boldsymbol{f}} = 0 \tag{31}$$

as is visualized in Fig. 2. Employing (14) we find that

$$0 = \partial_{\boldsymbol{f}} \phi \cdot \left[-\partial_{\boldsymbol{\varepsilon}} \psi : \dot{\boldsymbol{\varepsilon}} - \partial^2_{\boldsymbol{\xi}\boldsymbol{\xi}} \Psi^M \cdot \dot{\boldsymbol{\xi}} + \dot{\boldsymbol{\gamma}} - \dot{\delta} \boldsymbol{e}^* \right]. \tag{32}$$

Note that the restriction $\boldsymbol{\xi} \in \mathbb{P}^{n-1}$ forces the last two terms in this expression to be zero. The last term is zero by requirement (9) that the phase fractions sum to one, which implies by differentiation with respect to time that $\boldsymbol{e}^* \cdot \dot{\boldsymbol{\xi}} = 0$. Using Eq. (20) yields the result that the normal to the transformation surface during evolution must be orthogonal to $\boldsymbol{e}^*$; i.e. $\partial_{\boldsymbol{f}} \phi \cdot \boldsymbol{e}^* = 0$. The penultimate term is zero by the requirement that the phase fractions be non-negative. For phase fractions with inactive constraints ($\xi^\alpha \neq 0$ or $\xi^\alpha = 0$ and $\dot{\xi}^\alpha > 0$), the corresponding components of $\dot{\boldsymbol{\gamma}}$ will be zero; for those phase fractions that are zero and continue to be zero the evolution equation (20) will require the corresponding component of $\partial_{\boldsymbol{f}} \phi$ to be zero. The net result, is that

$$\partial_{\boldsymbol{f}} \phi \cdot \dot{\boldsymbol{\gamma}} = 0 \tag{33}$$

during phase evolution. Based on these observations and the introduction of Eq. (20) we can solve for the multiplier λ to give:

$$\lambda = -\frac{\partial_{\boldsymbol{f}} \phi \cdot \partial_{\boldsymbol{\varepsilon}} \psi : \dot{\boldsymbol{\varepsilon}}}{\partial_{\boldsymbol{f}} \phi \cdot \partial^2_{\boldsymbol{\xi}\boldsymbol{\xi}} \Psi^M \cdot \partial_{\boldsymbol{f}} \phi}. \tag{34}$$

Thus the stress rate may expressed in a symmetric form during active evolution entirely in terms of the present state and the rate of change of the strain:

$$\dot{\boldsymbol{\sigma}} = \left[\mathbb{C} - \frac{\partial_{\boldsymbol{f}} \phi \cdot \partial_{\boldsymbol{\varepsilon}} \psi \otimes \partial_{\boldsymbol{f}} \phi \cdot \partial_{\boldsymbol{\varepsilon}} \psi}{\partial_{\boldsymbol{f}} \phi \cdot \partial^2_{\boldsymbol{\xi}\boldsymbol{\xi}} \Psi^M \cdot \partial_{\boldsymbol{f}} \phi} \right] : \dot{\boldsymbol{\varepsilon}}. \tag{35}$$

Clearly, in the case of no evolution, $\lambda = 0$, one merely retains the first term inside the square brackets.

2.6 Discussion

The model that appears in the previous sections is formally similar to that of classical plasticity with the notable exception of the constraints on the evolution of the internal kinematic-like variables $\boldsymbol{\xi}$. These constraints are embodied in the multipliers $\boldsymbol{\gamma}$ and δ. The geometric picture that emanates from these equations is as follows. The conjugate forces, $\boldsymbol{f}$, are constrained to a convex domain in $\mathbb{R}^n$. Active evolution can only take place when the force $\boldsymbol{f}$ is on the boundary of the convex domain. When evolution takes place the rate of change of the force, $\dot{\boldsymbol{f}}$, obviously must lie in the tangent space to the transformation domain. To this point the picture is exactly as in classical plasticity. However, the presence of the requirement $\boldsymbol{\xi} \in \mathbb{P}^{n-1}$ provides further restrictions. In particular, since Eq. (9) must hold at all times, so must its time derivative. This implies that during evolution the force must lie at a point on the transformation surface where the normal is in the hyperplane orthogonal to $\boldsymbol{e}^*$; this is visualized in Fig. 2 for the case of the 2-norm. This forces $\dot{\boldsymbol{f}}$ to be in the space orthogonal to both $\boldsymbol{e}^*$ and $\partial_{\boldsymbol{f}}\phi$. Further, since Eq. (10) must also hold and a component of $\boldsymbol{\gamma}$ can not be changing unless the corresponding component of $\boldsymbol{\xi}$ is zero, we have the added restriction that evolution points of the transformation surface must have a normal in the hyperplane orthogonal to $\boldsymbol{\gamma}$. The intersection of these conditions defines a markedly reduced set of points on the transformation surface where transformation can actually take place. Other points on the transformation surface are in a sense inaccessible for purposes of evolution in the model. This occurs because as one tries to approach these other points, it is always possible to choose admissible values for δ and $\boldsymbol{\gamma}$ that keep the norm of $\boldsymbol{f}$ strictly less than f_c and thus λ is forced to be zero and no evolution can take place. These observations are explicitly exploited in the numerical approximation to the model.

Part of the reason for this situation is the fact that we have chosen not to eliminate one of the phase fractions from the model as we could have easily done using the constraint on the sum of the phase fractions being unity. This is the cause for the first requirement of a transformation surface normal to be in a hyperplane orthogonal to $\boldsymbol{e}^*$. It is worth pointing out that we avoid the urge to work in a reduced dimensional space on two grounds: (1) We prefer to work in the natural coordinates of pure phase fractions where no variant is given a preferential treatment by its elimination. (2) By working in the full space we actually simplify some of the geometry of the evolution.

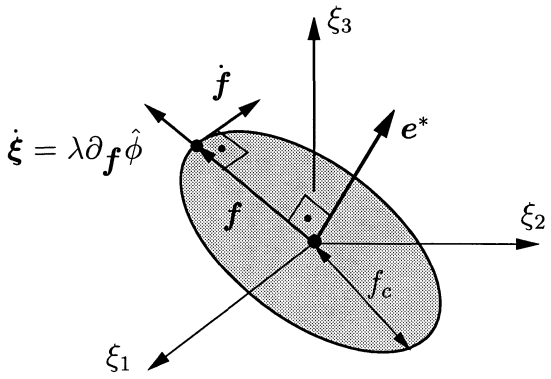

Figure 2: Elastic conjugate force domain and transformation surface. The thermodynamic force $\boldsymbol{f}$ is constrained to lie in the elastic domain $\mathbb{E} \subset \mathbb{R}^n$. Phase transformation can take place for points $\boldsymbol{f}$ on the transformation surface $\partial\mathbb{E}$. For $n = 3$ and the 2-norm, the entire set $\mathbb{E}$ is orthogonal to $\boldsymbol{e}^*$ as shown.

This is especially true when trying to view the model when the chosen norm is a p-norm with $\infty > p > 2$.

The more interesting restriction that is associated with the constraint of positive phase fractions is more fundamental to the modeling of martensites and can not be avoided. Its geometric picture is more complicated to explain and we defer that discussion to the section on time integration where its meaning is slightly more transparent.

3 Time Integration

In this section we discuss the time integration of the constitutive model outlined in the previous section. In particular, we focus on the integration of the constitutive model under strain and temperature control as is common in the majority of FEM codes. Thus we assume the entire state of the material is known at a time t_n and we wish to advance the state to time $t_{n+1} = t_n + \Delta t$, where $\Delta t > 0$ and $\boldsymbol{\varepsilon}_{n+1}$ and θ_{n+1} are given. For ease of discussion and presentation, we will mainly consider the case of a C^1 transformation surface.

Table 2: Summary of Discrete Equations to be solved at t_{n+1}

Transformation Criteria	
$\phi(\boldsymbol{f}) = \|\boldsymbol{f}\| - f_c \leq 0$	(36)
$\Delta\lambda\phi = 0$	(37)
$\Delta\lambda \geq 0$	(38)
Conjugate Force	
$\boldsymbol{f} + \boldsymbol{\psi}(\boldsymbol{\varepsilon}) - \boldsymbol{\gamma} + \partial_{\boldsymbol{\xi}}\Psi^M(\boldsymbol{\xi}) + \delta\boldsymbol{e}^* = 0$	(39)
Evolution Equation	
$\boldsymbol{\xi} - \boldsymbol{\xi}_n - \Delta\lambda\partial_{\boldsymbol{f}}\phi = 0$	(40)
Polytope Constraint	
$-\boldsymbol{\xi} \leq 0$	(41)
$-\boldsymbol{\gamma} \cdot \boldsymbol{\xi} = 0$	(42)
$\boldsymbol{\gamma} \geq 0$	(43)
$\boldsymbol{e}^* \cdot \boldsymbol{\xi} - 1 = 0$	(44)

3.1 Backward Euler

To integrate the equations we first apply a finite difference method to the evolution equation (26). Then we require all the remaining constitutive equations to be satisfied at time t_{n+1}. This results in a set of algebraic equations that must be solved for $(\boldsymbol{f}_{n+1}, \lambda_{n+1}, \boldsymbol{\gamma}_{n+1}, \delta_{n+1}, \boldsymbol{\xi}_{n+1})$. For specificity we will work with the Backward Euler method which is first order accurate and unconditionally A-stable. In classical plasticity this method has been shown to be B-stable (Simo and Govindjee [36]); in the present context this has not been shown yet but we believe it to be so. The discrete equations to be solved are summarized in Table 2 where for clarity we utilize the subscript indicating time only on quantities at time t_n and omit it for quantities at time t_{n+1}. In keeping with the conventions of computational plasticity, we designate $\Delta\lambda \equiv \Delta t\lambda$.

3.2 Active Set Solution Strategy

To solve the equations in Table 2 we must for a given value of $\boldsymbol{\varepsilon}$ determine the independent variables $(\Delta\lambda, \boldsymbol{\gamma}, \delta)$. Knowing these three quantities allows us to determine all the other relevant quantities in the Table. The fundamental difficulty is associated with the fact that one does not *a priori* know which variants will have active constraints associated with the $-\boldsymbol{\xi} \leq 0$ condition. This implies that one needs to have an active set strategy for solving the equations which are in general non-linear. The strategy that we find most robust is one where we first guess the set of active constraints as

$$B = \{\alpha \mid \xi_n^\alpha = 0\}\,. \tag{45}$$

Having guessed B, we then completely solve the constitutive equations, and then check the constraints. The set B is then adjusted using the following two rules:

1. All phase fractions with negative components in $\boldsymbol{\gamma}$ are removed from B.

2. The most negative phase fraction, if any, and those of equal numerical value are added to the set B.

The equations are then re-solved and the constraints re-checked until all equations have been satisfied. In what follows we discuss the issue of solving the equations in Table 2 for a *given active set* B with m active constraints. Because the set B may not be physically correct, the solution strategy must be able to handle *non-physical cases* such as negative $\boldsymbol{\gamma}$. Additional details regarding the active set procedure can be found in Appendix B.

3.3 Determination of an Elastic Time-step

The determination of an elastic time step is approached by an "elastic trial" method in the space of conjugate thermodynamic forces. During an elastic step no evolution of the phase fractions takes place and thus for an elastic step $\Delta\lambda = 0$. In such a situation, the discrete Kuhn-Tucker conditions require that $\|\boldsymbol{f}\| < f_c$. The question that arises is: *Is this possible?*

We can immediately eliminate this possibility if $\xi_n^\alpha \neq 0$ for some $\alpha \in B$. The reason for this is that for active constraints the phase fractions have to

be zero at t_{n+1}. Thus if ξ_n^α is not already zero for all $\alpha \in B$, then there must be phase evolution to satisfy the assumed active constraint.

If $\xi_n^\alpha = 0$ for $\forall \alpha \in B$, then we define a *trial elastic conjugate force* based on $\Delta\lambda = 0$:

$$\boldsymbol{f}^{tr} = -\boldsymbol{\psi}(\boldsymbol{\varepsilon}) + \boldsymbol{\gamma} - \partial_{\boldsymbol{\xi}} \Psi^M(\boldsymbol{\xi}_n) - \delta \boldsymbol{e}^* \,. \tag{46}$$

Unfortunately, this relation does not explicitly define $\boldsymbol{f}^{tr}$ due to the presence of δ and $\boldsymbol{\gamma}$. The multiplier δ can be removed by dotting Eq. (46) with $\boldsymbol{e}^*$ and solving for δ. If we plug this result back in, we obtain the following result:

$$\mathcal{P}^* \boldsymbol{f}^{tr} + \boldsymbol{s} = \mathcal{P}^* \boldsymbol{\gamma} \,, \tag{47}$$

where $\boldsymbol{s} = \mathcal{P}^*[\boldsymbol{\psi}(\boldsymbol{\varepsilon}) + \partial_{\boldsymbol{\xi}} \Psi^M(\boldsymbol{\xi}_n)]$, $\mathcal{P}^* = \mathbb{I} - \frac{1}{n} \boldsymbol{e}^* \otimes \boldsymbol{e}^*$ and $\mathbb{I}$ is the rank 2 identity tensor on $\mathbb{R}^n$. Note that we need not invoke Eq. (44) to determine δ since we are assuming an elastic step and that the state at time t_n completely satisfies the constitutive relations. While we still do not know what $\boldsymbol{\gamma}$ is, our original question can now be given the following geometric interpretation based on Eq. (47): An elastic step can occur if the known point $\boldsymbol{s}$ is within a f_c neighborhood of the projection of the positive span

$$\mathbb{K}^+ = \{\boldsymbol{x} \mid \boldsymbol{x} = \sum_{i \in B} \gamma_i \boldsymbol{e}_i \text{ and } \gamma_i \geq 0\} \tag{48}$$

onto the hyperplane orthogonal to $\boldsymbol{e}^*$; this is the set of points $\mathcal{P}^* \mathbb{K}^+$ as visualized in Fig. 3. Fig. 3 shows a case with two active constraints in B; in the figure d_1 denotes the distance of the point $\boldsymbol{s}$ to the projected positive span. In the definition of the positive span $\mathbb{K}^+$, $\boldsymbol{e}_i$ are the basis vectors of the canonical orthonormal basis on $\mathbb{R}^n$. One also needs to consider the possibility of a non-physical elastic step. This can arise during the active set selection process if too many phase fraction constraints are assumed to be active. Such a situation occurs, when there is a solution to Eq. (47) but with negative components in the vector $\boldsymbol{\gamma}$. To express this more precisely we can introduce the total span

$$\mathbb{K} = \{\boldsymbol{x} \mid \boldsymbol{x} = \sum_{i \in B} \gamma_i \boldsymbol{e}_i \text{ and } \gamma_i \in \mathbb{R}\} \,, \tag{49}$$

which is visualized in Fig. 4. Fig. 4 shows a case with one active constraint in B; in the figure d_2 is the distance from $\boldsymbol{s}$ to the projected span. A non-physical elastic step will take place if the known point $\boldsymbol{s}$ is within a f_c neighborhood of $\mathcal{P}^* \mathbb{K}$ and not within a f_c neighborhood of $\mathcal{P}^* \mathbb{K}^+$.

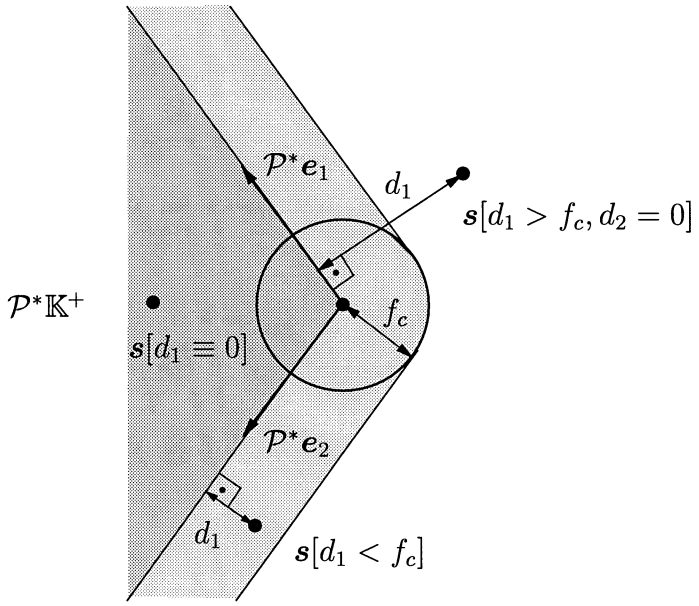

Figure 3: Underlying geometry of the proposed optimization algorithm for the case of three variants and two active constraints utilizing the 2-norm. Shown is $\boldsymbol{s}[d_1 = 0]$ and $\boldsymbol{s}[d_1 < f_c]$ implying elastic steps and $\boldsymbol{s}[d_1 > f_c\,,\, d_2 = 0]$ implying an incorrect active set.

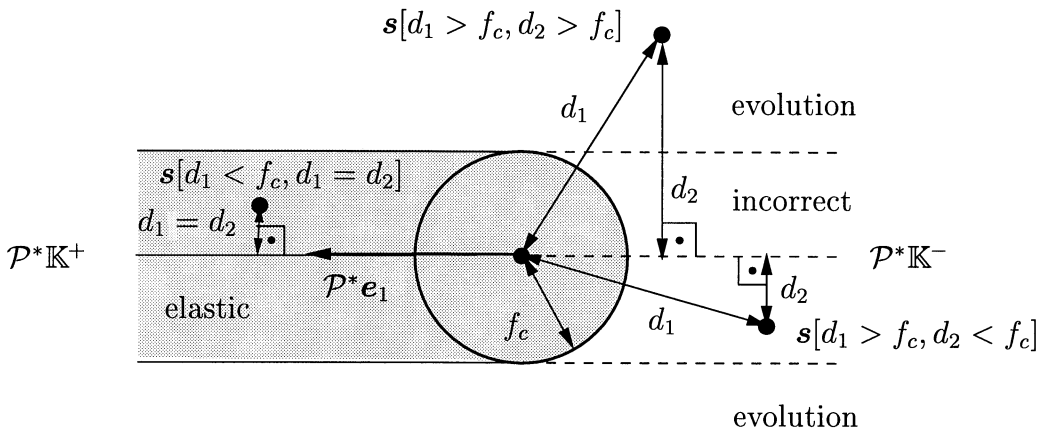

Figure 4: Underlying geometry of the proposed optimization algorithm for the case of three variants and *one* active constraints utilizing the 2-norm. Shown is $\boldsymbol{s}[d_1 < f_c\,,\, d_2 = d_1]$ implying an elastic step, $\boldsymbol{s}[d_1 > f_c\,,\, d_2 > f_c]$ implying evolution, $\boldsymbol{s}[d_1 > f_c\,,\, d_2 < f_c]$ implying an incorrect active set. $\mathbb{K}^- = \mathbb{K} \setminus \mathbb{K}^+$.

These statements can be understood by considering Figs. 3 and 4 which show the geometry for a variety of possible outcomes when one considers three variants and the 2-norm. Example points for $\boldsymbol{s}$ are shown in the figures. The distance to $\mathbb{K}^+$ is denoted in the Figures by d_1 and the distance to $\mathbb{K}$ is denoted by d_2. We are now led to the following 2 nonlinear programming problems for determining when an elastic step is taking place:

Constrained Elastic Minimization Problem 1:

$$d_1 = \min_{\boldsymbol{\gamma}_B \geq 0} \|\boldsymbol{s} - \boldsymbol{V}\boldsymbol{\gamma}_B\|\,, \tag{50}$$

where $\boldsymbol{V} = [\mathcal{P}^*\boldsymbol{e}_{B(1)} \cdots \mathcal{P}^*\boldsymbol{e}_{B(m)}]$, $\boldsymbol{\gamma}_B \in \mathbb{R}^m$, and $\boldsymbol{\gamma}_B \cdot \boldsymbol{w}_i = \boldsymbol{\gamma} \cdot \boldsymbol{e}_{B(i)}$. The $\boldsymbol{w}_i$ are the basis vectors of the canonical orthonormal basis of $\mathbb{R}^m$.

Unconstrained Elastic Minimization Problem 2:

$$d_2 = \min_{\boldsymbol{\gamma}_B} \|\boldsymbol{s} - \boldsymbol{V}\boldsymbol{\gamma}_B\|\,. \tag{51}$$

Based on these values of d_1 and d_2 we can provide the following elastic step selection algorithm:

Selection Algorithm: If $d_1 \leq f_c$ then the time step is elastic. If $d_1 > f_c$ and $d_2 \leq f_c$ then the step is a non-physical elastic step with some negative $\boldsymbol{\gamma}$'s.

In the case of the 2-norm the stated problems are classical quadratic programming problems and can be easily solved using standard methods. Methods for solving Eq. (50) are discussed in Luenberger [30, §14.3] and Bertsekas [8]; Eq. (51) is simply solved via a direct solution of the normal equations. It is noted in both cases that the problem is very well posed as the columns of $\boldsymbol{V}$ are nearly orthogonal. In fact the dot product between any two columns is equal to $-\frac{1}{n}$. It is also noted that the needed normal operator and its inverse for the solution of the quadratic programming problems can be given in closed form. The algorithmic details for the case of the 2-norm are given in Appendix A. For more general norms, the problems are still well behaved and can be solved via iteration; see again Luenberger [30] and Bertsekas [8].

3.4 Evolution:

Only in the cases where $d_1 > f_c$ and $d_2 > f_c$ or $\xi_n^\alpha \neq 0$ for any $\alpha \in B$ can $\Delta\lambda$ be non-zero and evolution of the phase fractions take place. In these cases there are $n+m+2$ unknowns to be determined from the following $n+m+2$ equations:

$$\boldsymbol{f} + \boldsymbol{\psi}(\boldsymbol{\varepsilon}) - \boldsymbol{\gamma} + \partial_{\boldsymbol{\xi}} \Psi^M(\boldsymbol{\xi}_n + \Delta\lambda \partial_{\boldsymbol{f}} \phi) + \delta \boldsymbol{e}^* = 0 \tag{52}$$

$$\xi_n^\alpha + \Delta\lambda \partial_{f^\alpha} \phi = 0 \qquad \alpha \in B \tag{53}$$

$$\phi(\boldsymbol{f}) = \|\boldsymbol{f}\| - f_c = 0 \tag{54}$$

$$\boldsymbol{e}^* \cdot (\boldsymbol{\xi}_n + \Delta\lambda \partial_{\boldsymbol{f}} \phi) - 1 = 0 \tag{55}$$

In general the equations are non-linear and need to be approached using an iterative technique such as Newton Method. When considering p-norms only the infinity norm yields a system of linear equations; this simplification, however, is offset by the need to introduce an additional active set search due to the introduction of the sub-differential. In the examples below we use full Newton with line-search to solve these equations. If the unknowns are collected in a single vector $\boldsymbol{X} \in \mathbb{R}^{n+m+2}$ in the following order $\boldsymbol{X} := (\boldsymbol{f}, \boldsymbol{\gamma}_B, \Delta\lambda, \delta)$ and the residual equations are collected into a single

vector $\boldsymbol{R} \in \mathbb{R}^{n+m+2}$ in the order shown in Eqs. (52)–(55), then the necessary iteration tangent is given by

$$\boldsymbol{K} = \frac{\partial \boldsymbol{R}}{\partial \boldsymbol{X}} = \begin{bmatrix} \mathbb{I} + \Delta\lambda \partial^2_{\boldsymbol{\xi}\boldsymbol{\xi}} \Psi^M(\boldsymbol{\xi}) \cdot \partial^2_{\boldsymbol{f}\boldsymbol{f}} \phi & -\mathbb{I}_B & \partial^2_{\boldsymbol{\xi}\boldsymbol{\xi}} \Psi^M(\boldsymbol{\xi}) \cdot \partial_{\boldsymbol{f}} \phi & \boldsymbol{e}^* \\ \Delta\lambda \partial^2_{\boldsymbol{f}_B \boldsymbol{f}} \phi & 0 & \partial_{\boldsymbol{f}_B} \phi & 0 \\ \partial_{\boldsymbol{f}} \phi & \boldsymbol{0} & 0 & 0 \\ \Delta\lambda \boldsymbol{e}^* \cdot \partial^2_{\boldsymbol{f}\boldsymbol{f}} \phi & \boldsymbol{0} & \boldsymbol{e}^* \cdot \partial_{\boldsymbol{f}} \phi & 0 \end{bmatrix} . \tag{56}$$

Here $\boldsymbol{f}_B \in \mathbb{R}^m$ and $\boldsymbol{f}_B \cdot \boldsymbol{w}_i = f_{B(i)}$. $\mathbb{I}_B \in \mathbb{R}^{n \times m}$ and $\boldsymbol{e}_i \cdot \mathbb{I}_B \boldsymbol{w}_j = 1$ for $i = B(j)$ and zero otherwise.

3.5 Global Tangent Operator

For general finite element computations the variation of the stress is needed with respect to the strain for the global equilibrium solution. Since the constitutive equations are evaluated using an algorithm, the continuum tangent operator (35) will not lead to quadratic convergence when utilizing a Newton method on the global level. The variation of the algorithm itself is needed for this purpose (Simo and Taylor [38]). For the two possible elastic steps this is just the elastic tangent. In the case of evolution, we can take the variation of the stress with respect to the strain to give

$$\delta\boldsymbol{\sigma} = \sum_{\alpha=1}^{n} \xi^\alpha \mathbb{C} : \delta\boldsymbol{\varepsilon} + \sum_{\alpha=1}^{n} \delta\xi^\alpha \mathbb{C} : (\boldsymbol{\varepsilon} - \boldsymbol{\varepsilon}^\alpha) \tag{57}$$

$$= \mathbb{C} : \delta\boldsymbol{\varepsilon} + \sum_{\alpha=1}^{n} \delta\xi^\alpha \boldsymbol{\sigma}^\alpha . \tag{58}$$

The variation of the phase fractions is given by the discrete evolution law as:

$$\delta\boldsymbol{\xi} = \delta(\boldsymbol{\xi}_n + \Delta\lambda \partial_{\boldsymbol{f}} \phi) \tag{59}$$

$$= \delta\Delta\lambda \partial_{\boldsymbol{f}} \phi + \Delta\lambda \partial^2_{\boldsymbol{f}\boldsymbol{f}} \phi \cdot \delta\boldsymbol{f} . \tag{60}$$

The variation of the incremental multiplier $\Delta\lambda$ and the conjugate force $\boldsymbol{f}$ are found by taking the variation of the residual equations (52)–(55) with

respect to the strain. This yields the system of equations

$$\boldsymbol{K}\begin{bmatrix} \delta \boldsymbol{f} \\ \delta \boldsymbol{\gamma}_B \\ \delta \Delta\lambda \\ \delta\delta \end{bmatrix} = \begin{bmatrix} -\partial_{\boldsymbol{\varepsilon}} \boldsymbol{\psi} : \delta\boldsymbol{\varepsilon} \\ \boldsymbol{0} \\ 0 \\ 0 \end{bmatrix} \tag{61}$$

By noting that $\boldsymbol{e}_\alpha \cdot [\partial_{\boldsymbol{\varepsilon}} \boldsymbol{\psi} : \delta\boldsymbol{\varepsilon}] = \boldsymbol{\sigma}^\alpha : \delta\boldsymbol{\varepsilon}$ we can write the desired tangent operator as

$$\mathbb{C}^{\text{algo}} = \mathbb{C} - \sum_{\substack{\alpha=1 \\ \beta=1}}^{n} D_{\alpha\beta} \boldsymbol{\sigma}^\alpha \otimes \boldsymbol{\sigma}^\beta \,, \tag{62}$$

where $D_{\alpha\beta}$ are the components of a symmetric rank-2 tensor on $\mathbb{R}^n$ which is given as

$$\boldsymbol{D} = \partial_{\boldsymbol{f}} \phi \otimes \boldsymbol{v} + \Delta\lambda \partial^2_{\boldsymbol{f}\boldsymbol{f}} \phi \cdot \boldsymbol{A} \,. \tag{63}$$

$\boldsymbol{v}$ is a vector whose components are the first n values of the $(n+m+1)^{\text{th}}$ row of $\boldsymbol{K}^{-1}$, and $\boldsymbol{A}$ is the upper-left $n \times n$ block of $\boldsymbol{K}^{-1}$.

4 Examples

In this section we partially examine the behavior of the proposed material model and its numerical approximation. In particular we consider the experimental observations of Shield [35] during tension tests on single crystal CuNiAl specimens. This material undergoes a cubic to orthorhombic transformation and has 6 martensite variants and 1 austenite; i.e. $n = 7$. The mixing energy form that we adpot for the examples is the Reußlower bound. The experiments details are given by Shield and are not repeated here. We merely note that the essential experiment was a tension test with unloading on single crystal specimens with different orientations. Reported data includes among other items stress-strain loops, observations of martensitic variants, and Young's moduli for different orientations. Below we examine the ability of the model to predict orientational changes in the stress strain behavior, the production of correct martensitic variants, and its general numerical behavior.

For the numerical comparisons we concentrate on the tension tests with clamped-clamped end conditions. The specimen utilized by Shield was dog-bone shaped. In our comparisons we utilized a simpler rectangular geometry

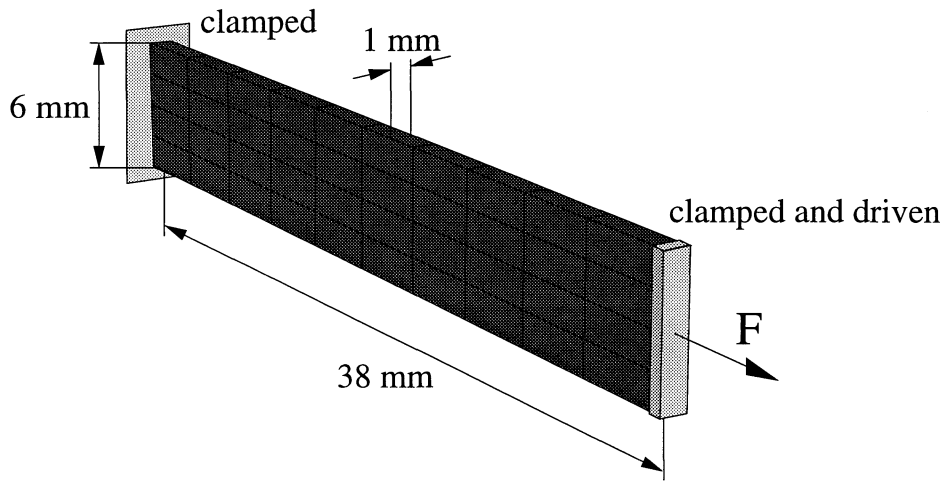

Figure 5: Chosen geometry and boundary conditions for simulations. Shown are 8-node fully integrated displacement formulation bricks.

since not all the relevant details of experimental set-up are reported in the paper; see Fig. 5. In particular, we note that many of the fine details of the simulations that are shown below are sensitive to end conditions on the tested material. Thus in what follows, we also make no great attempt to fit the reported data. Our interest is only in showing that the model without much effort can give modestly accurate predictions of stress-strain behavior as well as detailed microstructural information.

The precise material property values used in the simulations are given in Table 3. The values of the critical transformation force and the well minima were chosen to roughly produce the stress-strain loop for specimen T1-A3b. It is noted that the well heights control the stresses at which transformations takes place and the critical force controls the amount of hysteresis seen. The Poisson's ratio was chosen to simply be something reasonable for a metal (isotropy is assumed throughout). The remaining properties are as reported in Shield [35]. The transformation strains are generated from the data given in the Table 3 by computing the transformation right stretch tensors, $\boldsymbol{U}^\alpha$, for the martensites using the relations given in Bhattacharya and Kohn [9, 10]; for the austenite $\boldsymbol{U}^\alpha$ is the identity. The transformation strains are then taken as $\boldsymbol{\varepsilon}^\alpha = \frac{1}{2}(\boldsymbol{U}^{\alpha^2} - \mathbf{1})$. Lastly the transformation strains are rotated into the proper orientation as $\boldsymbol{\varepsilon}^\alpha = \boldsymbol{Q}\boldsymbol{\varepsilon}^\alpha\boldsymbol{Q}^T$, where $\boldsymbol{Q} \in SO(3)$ is such that its first row is $\boldsymbol{t}^1$, its second $\boldsymbol{t}^2$, and its third $\boldsymbol{t}^1 \times \boldsymbol{t}^2$.

Table 3: Material Properties for Simulations

f_c	0.9 N-mm/mm^3
Poisson's Ration	0.25
M^α	(-7.0, 0.0, 0.0, 0.0, 0.0, 0.0, 0.0) N-mm/mm^3
Young's Modulus A1-T1b	26,700 N/mm^2
Young's Modulus A1-T2b	72,000 N/mm^2
Young's Modulus A1-T3b	158,000 N/mm^2
Principal Transformation Stretches	(1.0619, 0.9178, 1.0230)
Cubic Axes A1-T1b	$\boldsymbol{t}^1$ =(0.925, 0.380, 0.0)
	$\boldsymbol{t}^2$ =(-0.380, 0.925, 0.0)
Cubic Axes A1-T2b	$\boldsymbol{t}^1$ =(-0.477, -0.477, 0.775)
	$\boldsymbol{t}^2$ =(0.707, -0.707, 0.0)
Cubic Axes A1-T3b	$\boldsymbol{t}^1$ =(-0.577, -0.577, 0.577)
	$\boldsymbol{t}^2$ =(0.707, -0.707, 0.0)

4.1 Stress Strain Response

The top of Fig. 6 shows the data of Shield [35] for 3 of his specimens. The bottom of Fig. 6 shows the results from the proposed model. The parameters as mentioned before are visually adjusted to roughly correspond to specimen A1-T3b. The lowering of the transformation stress with orientation and the decrease in hysteresis with orientation are all natural products of the model. They appear without "tuning" of any kind. The inhomogeneous distribution of the austenite in the bar is shown in Fig. 7 for specimen A1-T3b at three different times during the forward transformation process – once near the start, once in the middle, and once near the completion.

4.2 Phase fraction histories

Shown in Figs. 8, 9, and 10 are the time histories of the phase fractions for a single Gauß point close to the center of the specimen. As was observed by Shield [35] certain martensite variant combinations appear during the phase transformation process. These combinations correspond to those that are computed from the theory of martensites see Wechsler, Liebermann, and Read [44], Ball and James [6, 7]; see also Shield [35]. For specimens A1-T2b and A1-T3b, the proposed model correctly predicts the experimentally observed production under load of martensite variants $(2, 6)$ and $(2, 3, 6)$,

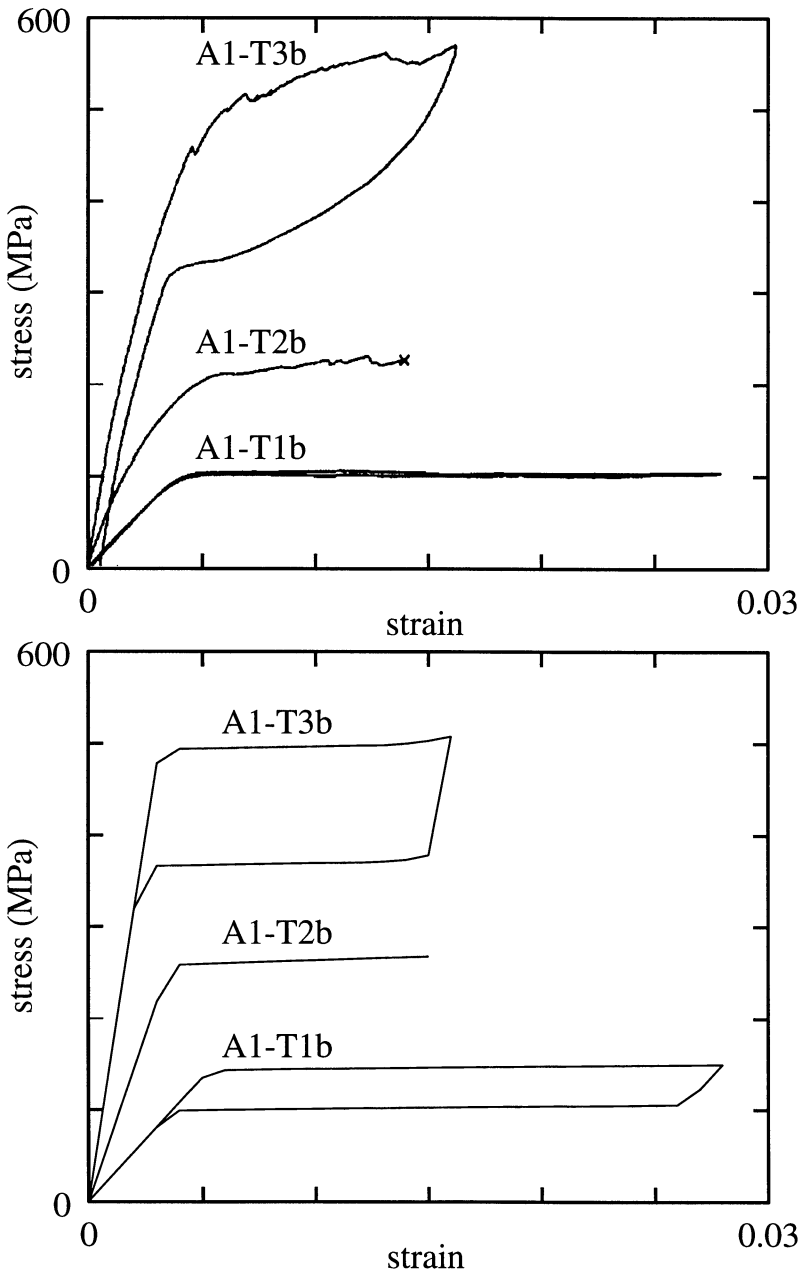

Figure 6: Stress Strain response for 3 different crystal orientations. Top: Experimental data of Shield [35]. Bottom: Model output. The model results are loosely adjusted to correspond to A1-T3b. The results for A1-T2b and A1-T1b are then predicted by the model using this fixed data set.

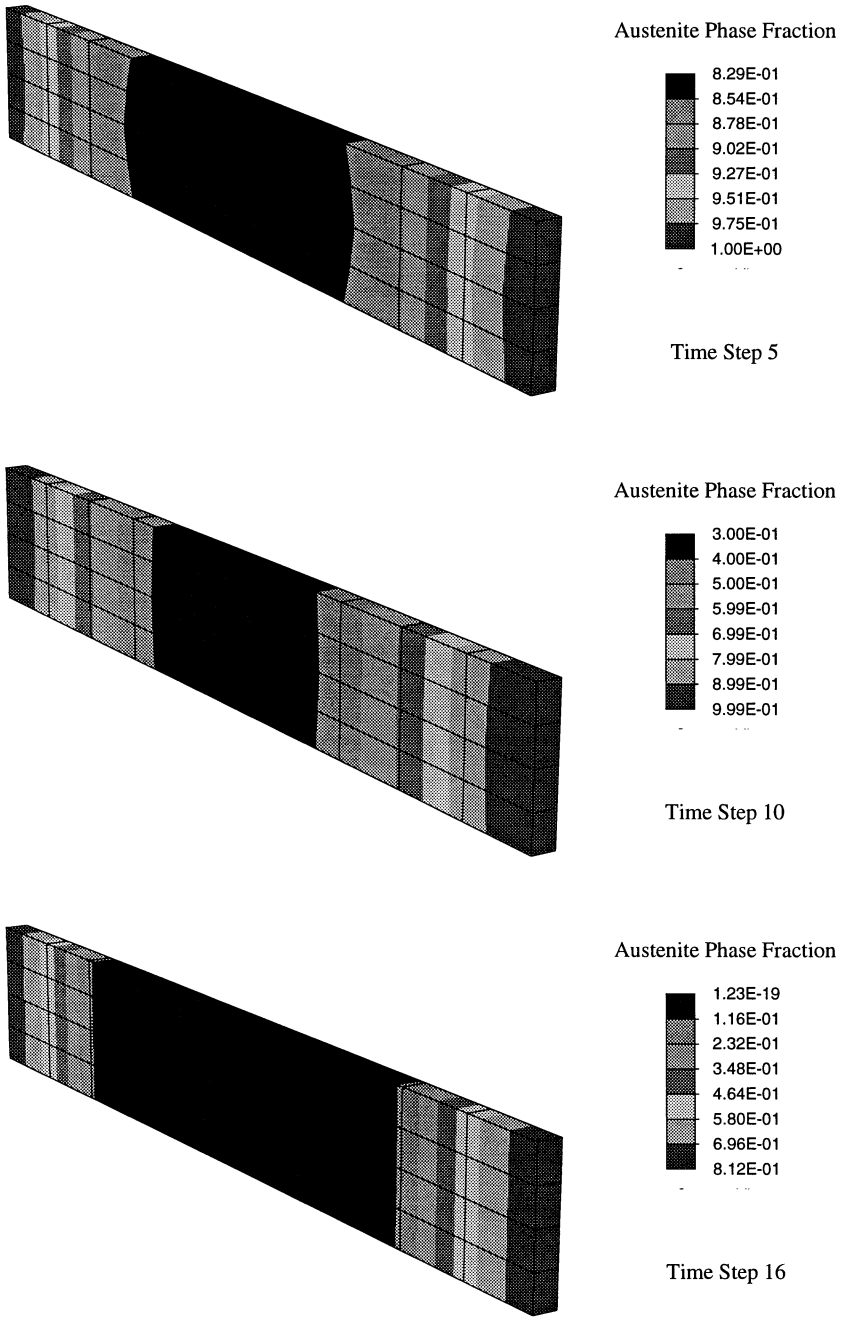

Figure 7: Inhomogeneous distribution of austenite in A1-T3b specimen at time step 5, 10, and 16. Note the strong gradient at the end of the bar.

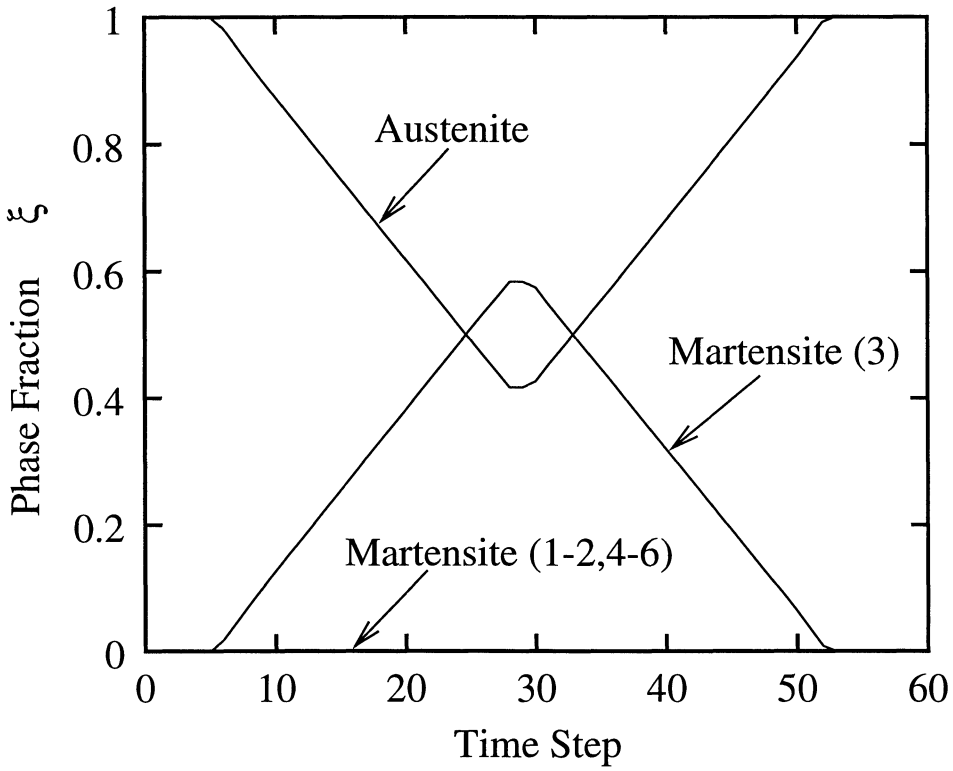

Figure 8: Phase fraction histories for an element in the center of test specimen A1-T1b.

respectively. The numbering convention is that of Shield [35]. For specimen A1-T1b, Shield observed martensite variants $(1, 2, 3)$. We, however, only find variant 3 in the center of the bar in our evolutionary simulations. The most likely cause for this discrepancy is that our mixing free energy is a lower bound. This has the effect of permitting lower energies of mixing of variant 3 with the austenite than are realistic. This then provides for a false low energy path of evolution for the model. With a higher value of the mixing energy between variant 3 and the austenite the system would presumably move into a twinned martensite state such as what we observe for the other two specimen orientations.

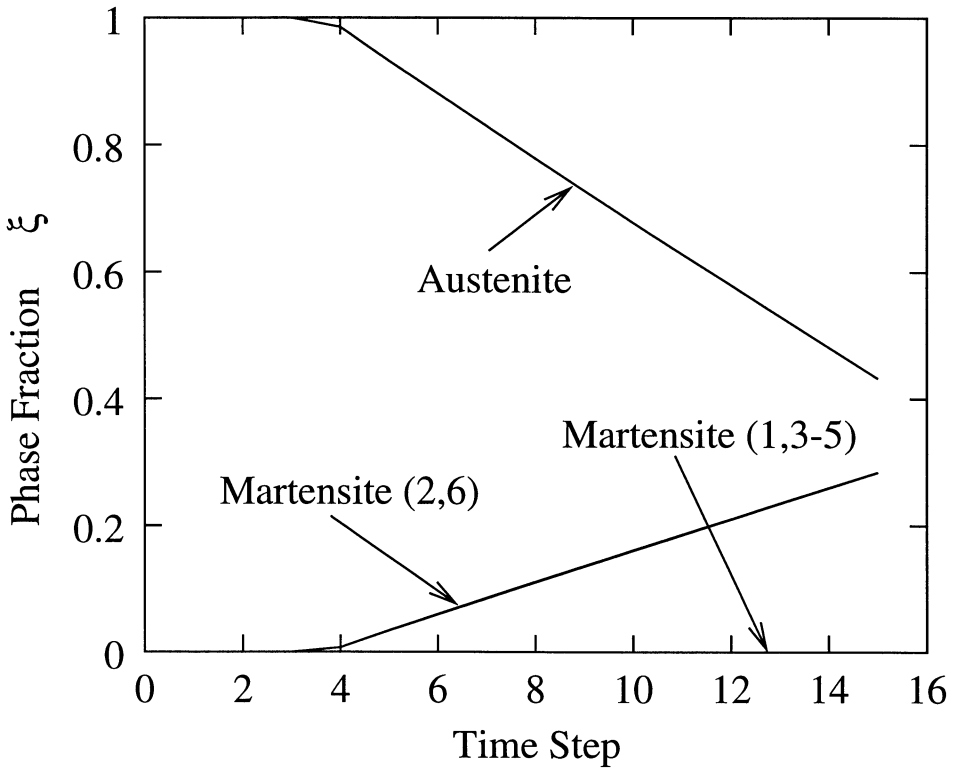

Figure 9: Phase fraction histories for an element in the center of test specimen A1-T2b.

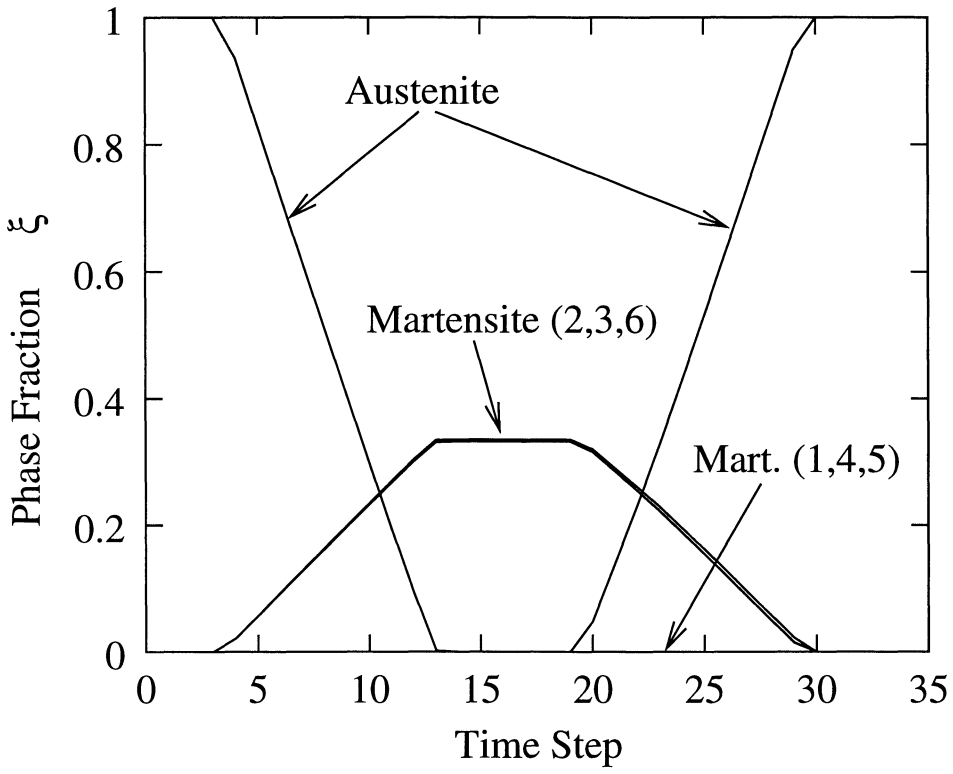

Figure 10: Phase fraction histories for an element in the center of test specimen A1-T3b.

Table 4: Typical global residual norm patterns for specimen A1-T3b. Superscript numbers indicate the number of line searches performed during the time step.

Global Iteration	Residual Norm		
	Time Step 5	Time Step 10	Time Step 16
1	6.2515596E+03	6.2346314E+03	5.6211250E+03
2	1.8463011E+02	1.7456376E+02	1.4111144E+03
3	4.7733559E+02	1.9988936E+02[1]	5.6113686E+01
4	9.1232153E+01	4.1771859E+01	2.8559476E+01[2]
5	8.4598797E+01[1]	3.3998000E+01	2.0835611E+01
6	5.1326364E+01	3.7914935E+01[1]	1.6620460E+01[3]
7	2.2723693E+01	1.2553766E+01	1.0787363E+01
8	8.6149914E+00	1.4303171E+00	1.0336966E+00
9	3.8917006E+00	5.4039193E-02	1.9291230E-07
10	8.2638571E-01	1.5377304E-04	
11	5.4361158E-02	9.8204387E-10	
12	2.3645387E-04		
13	4.5677205E-09		

4.3 Global Convergence Behavior

Shown in Table 4 are the global residual patterns from the FEM simulation on specimen A1-T3b at the same time steps as were shown in Fig. 7. The computation was carried out using a symmetric full Newton solver with line search. There were 16 time steps during the loading and 16 on the unloading. Thus the time step sizes are moderate in size. Clearly the global equations are somewhat difficult to solve but once the solution is approached the iteration procedure shows quadratic convergence. Most of this difficulty arises from the very constrained conditions at the end of the bar where Newton's method has some difficulty in finding the solution.

5 Closure

In this paper, we have developed a model for the simulation of the evolution of the martensitic structure of alloys. The model has a distinct geometric structure which we have been able to exploit for the purposes of understand-

ing the model as well as constructing a viable numerical approximation to it. Without a clear geometric picture, the development of the algorithm would not have been possible. Overall the predictions of the model are quite surprisingly good even though many important issues have not been explicitly dealt with. In particular the model is seen to generate naturally orientation dependent results and most importantly the model is seen to generate the correct (observed) martensite combinations. This occurs in spite of the fact that we have ignored issues of finite deformation and elastic anisotropy. These last two points are the subject of on going research as is research into the behavior of the model when coupled to heat transfer.

Acknowledgements

SG dankt der Alexander von Humboldt–Stiftung für die Verleihung eines Forschungsstipendium an der Universität Stuttgart. SG also acknowledges the support of the Lawrence Livermore National Laboratory through subcontract B502681 of DOE prime contract W-7405-ENG-48.

References

[1] R. Abeyaratne, S-J. Kim, and J.K. Knowles, *A one-dimensional continuum model for shape-memory alloys*, International Journal of Solids and Structures **31** (1994), 2229–2249.

[2] R. Abeyaratne and S.J. Kim, *Cyclic effects in shape-memory alloys: A one-dimensional continuum model*, International Journal of Solids and Structures **34** (1997), 3273–3289.

[3] M. Achenbach, *A model for an alloy with shape memory*, International Journal of Plasticity **5** (1989), 371–395.

[4] M. Achenbach, T. Atanackovic, and I. Müller, *A model for memory alloys in plane strain*, International Journal of Solids and Structures **22** (1986), 171–193.

[5] M. Achenbach and I. Müller, *Simulation of material behavior of alloys with shape memory*, Archives of Mechanics **35** (1985), 537–585.

[6] J.M. Ball and R.D. James, *Fine phase mixtures as minimizers of energy*, Archive for Rational Mechanics and Analysis **100** (1987), 13–52.

[7] ———, *Proposed experimental tests of a theory of fine microstructures and the 2-well problem*, Philosophical Transactions of the Royal Society of London **A338** (1992), 389–450.

[8] D.P. Bertsekas, *Nonlinear programming*, Athena Scientific, 1995.

[9] K. Bhattacharya and R.V Kohn, *Recoverable strains in shape-memory alloys*, Journal de Physique IV **5** (1995), C8–261–C8–266.

[10] ———, *Symmetry, texture and the recoverable strain of shape-memory polycrystals*, Acta Materiallia **44** (1996), 529–542.

[11] Z. Bo and D.C. Lagoudas, *Thermomechanical modeling of polysrystalline SMAs under cyclic loading, Part I: theoretical derivations*, International Journal for Engineering Science **37** (1999), 1089–1140.

[12] J.G. Boyd and D.C. Lagoudas, *A thermodynamic constitutive model for the shape memory materials. Part I. The monolithic shape memory alloy*, International Journal of Plasticity **12** (1996), 805–842.

[13] ———, *A thermodynamic constitutive model for the shape memory materials. Part II. The SMA composite material*, International Journal of Plasticity **12** (1996), 843–873.

[14] L.C. Brinson and R. Lammering, *Finite element analysis of the behavior of shape memory alloys and their applications*, International Journal of Solids and Structures **30** (1993), 3261–3280.

[15] B.D. Coleman and M.E. Gurtin, *Themodynamics with internal state variables*, The Journal of Chemical Physics **47** (1967), 597–613.

[16] T.W. Duerig, K.N. Melton, D. Stockel, and C.M. Wayman, *Engineering aspect of shape memory alloys*, Butterworth-Heinemann, Boston, 1990.

[17] H. Funakubo, *Shape memory alloys*, Gordon and Breach Science Publishers, 1984, Translated by Kennedy, J.B.

[18] X. Gao, M. Huang, and L.C. Brinson, *A multivariant micromechanical model for SMAs Part 1: Crystallographic issues for single crystal model*, International Journal of Plasticity, (to appear).

[19] S. Govindjee and G.J. Hall, *Computational aspects of solid-solid phase transformation modeling with a Gibbs functions*, Smart Structures and Materials 1999: Mathematics and Control in Smart Structures, Proceedings of SPIE (Vasundara V. Varadan, ed.), vol. 3667, SPIE Press, 1999, pp. 302–313.

[20] ———, *A computational model for shape memory alloys*, International Journal of Solids and Structures **37** (1999), 735–760.

[21] S. Govindjee and E.P. Kasper, *Computational aspect of one-dimensional shape memory alloy modeling with phase diagrams*, Computer Methods in Applied Mechanics and Engineering **171** (1999), 309–326.

[22] S. Govindjee and A. Mielke, *The free-energy of mixing for evolving martensitic materials by quasi-convex analysis*, (2000), (in preparation).

[23] G.J. Hall and S. Govindjee, *A model and numerical framework for the simulation of solid-solid phase transformations*, Tech. Report UCB/SEMM-1999/11, University of California Berkeley, Department of Civil Engineering, 1999.

[24] K.F. Hane and T.W. Shield, *Microstructure in the cubic to monoclinic transition in Titanium–nickel shape memory alloys*, Acta Materialia **47** (1999), 2603–2617.

[25] M. Huang and L.C. Brinson, *A multivariant model for single crystal shape memory alloy behavior*, Journal of the Mechanics and Physics of Solids **46** (1998), 1379–1409.

[26] A.V. Idesman, V.I. Levitas, and E. Stein, *Elastoplastic materials with martensitic phase transition and twinning at finite strains: Numerical solution with the finite element method*, Computer Methods in Applied Mechanics and Engineering **173** (1999), 71–98.

[27] R.V. Kohn, *The relaxation of a double-well problem*, Continuum Mechanics and Thermodynamics **3** (1991), 193–236.

[28] V.I. Levitas, A.V. Idesman, and E. Stein, *Shape memory alloys: Micromechanical modeling and numerical analysis of structures*, Journal of Intelligent Materials, Sytems, and Structures, (in press).

[29] J. Lubliner and F. Auricchio, *Generalized plasticity and shape memory alloys*, International Journal of Solids and Structures **33** (1996), 991–1003.

[30] D.G. Luenberger, *Linear and nonlinear programming*, Addison-Wesley, 1984.

[31] J.J. Moreau, *Evolution problem associated with a moving convex set in a Hilbert space*, Journal of Differential Equations **26** (1977), 347–374.

[32] ———, *Application of convex analysis to the treatment of elastoplastic systems*, Lecture Notes in Mathematics: Applications of Methods of Functional Analysis to Problems in Mechanics (P. Germain and B. Nayroles, eds.), vol. 503, Springer Verlag, 1979, pp. 56–89.

[33] I. Müller and H. Xu, *On the pseudo-elastic hysteresis*, Acta Metallurgica **39** (1991), 263–271.

[34] M.A. Qidwai and D.C. Lagoudas, *Numerical implementation of a shape memory alloy thermomechanical constitutive model using return mapping algorithms*, International Journal for Numerical Methods in Engineering **47** (2000), 1123–1168.

[35] T.W. Shield, *Orientation dependence of the pseudoelastic behavior of single crystals of Cu-Al-Ni in tension*, Journal of the Mechanics and Physics of Solids **43** (1995), 869–895.

[36] J.C. Simo and S. Govindjee, *Non-linear B-stability and symmetry preserving return mapping algorithms for plasticity and viscoplasticity*, International Journal for Numerical Methods in Engineering **31** (1991), 151–176.

[37] J.C. Simo, J.G. Kennedy, and S. Govindjee, *Non-smooth multisurface plasticity and viscoplasticity. loading/unloading conditions and numerical algorithms*, International Journal for Numerical Methods in Engineering **26** (1988), 2161–2185.

[38] J.C. Simo and R.L. Taylor, *Consistent tangent operators for rate independent elastoplasticity*, Computer Methods in Applied Mechanics and Engineering **48** (1986), 101–118.

[39] N. Siredey, E. Patoor, M. Berveiller, and A. Eberhardt, *Constitutive equations for polycrystalline thermoelastic shape memory alloys. Part I: Intergranular interactions and behavior of the grain*, International Journal of Solids and Structures **36** (1999), 4289–4315.

[40] V.P. Smyshlyaev and J.R. Willis, *On the relaxation of a three-well energy*, Proceedings of the Royal Society of London A **455** (1998), 779–814.

[41] Q.-P. Sun and K.-C. Hwang, *Micromechanics constitutive description of thermoelastic martensitic transformations*, Advances in Applied Mechanics, vol. 31, Academic Press, 1994, pp. 249–298.

[42] K. Tanaka and R. Iwasaki, *A phenomenological theory of transformation superplasticity*, Ing. Arch. **51** (1985), 287–299.

[43] L. Tartar, *H-measures, a new approach for studying homogenization, oscillation and concentration effects in partial differential equations*, Proceedings of the Royal Society of Edinburgh A **115** (1990), 193–230.

[44] M.S. Wechsler, D.S. Liebermann, and T.A. Read, *On the theory of the formation of martensite*, Transactions AIME: Journal of Metals **197** (1953), 1503–1515.

A Algorithms for d_1 and d_2

A.1 d_1 2-norm

To solve for d_1 we employ the feasible set method described in detail in the text of Luenberger [30, §14.3]. The critical point of problem (50) is the same as the critical point to

$$\min_{\boldsymbol{\gamma}_B \geq 0} \left\{ \frac{1}{2} \boldsymbol{\gamma}_B \cdot \boldsymbol{V}^T \boldsymbol{V} \boldsymbol{\gamma}_B - \boldsymbol{V}^T \boldsymbol{s} \cdot \boldsymbol{\gamma}_B \right\}, \tag{64}$$

where $\boldsymbol{s} = \mathcal{P}^*[\boldsymbol{\psi}(\boldsymbol{\varepsilon}) + \partial_{\boldsymbol{\xi}} \Psi^M(\boldsymbol{\xi}_n)]$. This problem is solved for $\boldsymbol{\gamma}_B$ using an active set method; the solution point can then be used to evaluate d_1 using

the distance formula from (50). The active set here refers to the components of $\boldsymbol{\gamma}_B$ which are zero in the present optimization problem and should not be confused with the active set B used in the residual equations. For purposes of differentiation we will denote this new active constraint set by A; the multipliers associated with the active set A will be denoted as $\boldsymbol{\Theta} \in \mathbb{R}^p$, where p is the size of A. We further define $\boldsymbol{z}^* \in \mathbb{R}^p$ as the vector of all ones in the standard basis. The algorithm is as follows where the tolerances given are appropriate for a double precision implementation:

1. **Initialize:**

$$\begin{aligned} A &= \{1, 2, \cdots, m\} && (65)\\ F &= \emptyset && (66)\\ \boldsymbol{\gamma}_B &= 10^{-4} && (67)\\ p &= \text{size}[A] && (68)\\ \text{TOL}_1 &= 10^{-12} && (69)\\ \text{TOL}_2 &= 10^{-11} && (70) \end{aligned}$$

2. **Set up constraint matrix:**

$$\hat{\boldsymbol{A}} = \begin{bmatrix} \boldsymbol{w}_{A(1)}^T \\ \boldsymbol{w}_{A(2)}^T \\ \vdots \\ \boldsymbol{w}_{A(p)}^T \end{bmatrix} \tag{71}$$

3. **Get local multipliers:**

$$\boldsymbol{\Theta} = \left[\hat{\boldsymbol{A}}(\boldsymbol{V}^T\boldsymbol{V})^{-1}\hat{\boldsymbol{A}}^T\right]^{-1}\left\{-\hat{\boldsymbol{A}}(\boldsymbol{V}^T\boldsymbol{V})^{-1}\boldsymbol{V}^T\boldsymbol{s} - \hat{\boldsymbol{A}}\boldsymbol{\gamma}_B\right\}, \tag{72}$$

where

$$\left[\hat{\boldsymbol{A}}(\boldsymbol{V}^T\boldsymbol{V})^{-1}\hat{\boldsymbol{A}}^T\right]^{-1} = \mathbb{I} - \frac{1}{n-m+p}\boldsymbol{z}^* \otimes \boldsymbol{z}^* \tag{73}$$

and

$$(\boldsymbol{V}^T\boldsymbol{V})^{-1} = \mathbb{I} + \frac{1}{n-m}\boldsymbol{w}^* \otimes \boldsymbol{w}^*. \tag{74}$$

4. **Obtain search direction:**

$$\boldsymbol{d} = (\boldsymbol{V}^T\boldsymbol{V})^{-1}\left(\hat{\boldsymbol{A}}^T\boldsymbol{\Theta} + \boldsymbol{V}^T\boldsymbol{s}\right) - \boldsymbol{\gamma}_B \tag{75}$$

5. **Compute convergence tolerance:**

$$\begin{aligned} \text{MAG} &= \text{Max Order of Magnitude}[\hat{\boldsymbol{A}}^T\boldsymbol{\Theta}, \boldsymbol{V}^T\boldsymbol{s}, \boldsymbol{\gamma}_B] && (76)\\ \text{TOL}_3 &= \text{TOL}_2 \times \text{MAG} && (77) \end{aligned}$$

6. **Check convergence:** If $\|\boldsymbol{d}\| < \text{TOL}_3$, then GOTO 9, else continue.

7. **Line search to boundary of cone:**

$$\begin{aligned} g &= \min_{\alpha \in F} \left\{ 1, -\frac{\gamma_B^\alpha}{d(\alpha)} \right\} && (78)\\ \boldsymbol{\gamma}_B &= \boldsymbol{\gamma}_B + g\boldsymbol{d} && (79) \end{aligned}$$

8. **Reset active constraints:**

$$\begin{aligned} A &= \{\alpha \mid \boldsymbol{\gamma}_B^\alpha \leq \text{TOL}_1\} && (80)\\ F &= \{1, 2, \cdots, m\} \setminus A && (81)\\ p &= \text{size}[A] && (82)\\ & && (83) \end{aligned}$$

GOTO 2.

9. **Check for validity of $\boldsymbol{\gamma}_B$:** If $\gamma_{B_i} > -\text{TOL}_1$, then GOTO 11, else continue.

10. **Drop all active constraints with negative $\boldsymbol{\Theta}$:**

$$\begin{aligned} F &= F \cap \{\alpha \mid \Theta^\alpha < \text{TOL}_1\} && (84)\\ A &= \{1, 2, \cdots, m\} \setminus F && (85)\\ p &= \text{size}[A] && (86)\\ & && (87) \end{aligned}$$

GOTO 2.

11. **Converged, Compute d_1:**

$$d_1 = \|\mathcal{P}^*[\boldsymbol{\psi}(\boldsymbol{\varepsilon}) + \partial_{\boldsymbol{\xi}}\Psi^M(\boldsymbol{\xi}_n)] - \boldsymbol{V}\boldsymbol{\gamma}_B\| . \qquad (88)$$

A.2 d_2 2-norm

Here the optimization problem is unconstrained and quadratic. Thus the solution is simply given as the solution to the normal equations; i.e.,

$$\boldsymbol{\gamma}_B = (\boldsymbol{V}^T\boldsymbol{V})^{-1}\boldsymbol{V}^T\boldsymbol{s} \tag{89}$$

and

$$d_2 = \|\boldsymbol{s} - \boldsymbol{V}\boldsymbol{\gamma}_B\| . \tag{90}$$

See Eq. (74) for the closed form to the inverse of the normal operator.

B Overall algorithmic details

In this Appendix we describe the details of the overall algorithm used to solve the discrete constitutive equations including the details of the active set method. The tolerancing given is appropriate for use in double precision computations.

1. **Set main tolerance:** TOL $= 10^{-12}$
2. **No constraint case check:** Let $\boldsymbol{f}^{tr0} = -\boldsymbol{s}$. IF $\phi(\boldsymbol{f}^{tr0}) \leq$ TOL, then the step is elastic STOP. ELSE CONTINUE.
3. **Initialize active set:** $B = \{\alpha \mid \xi_n^\alpha < \text{TOL}\}$
4. **Elastic non-linear programming problem:** IF $B \neq \emptyset$ and $\xi_n^\alpha <$ TOL for all $\alpha \in B$, then compute d_1 and d_2 as described in Appendix A. ELSE GOTO step 6.
5. **Elastic checks:** IF $d_1 \leq f_c$ and $\xi_n^{B(\alpha)} <$ TOL, then the step is elastic. Set

$$\boldsymbol{\xi} = \boldsymbol{\xi}_n \tag{91}$$
$$\gamma_{B(\alpha)} = \gamma_B^\alpha , \tag{92}$$

   where $\boldsymbol{\gamma}_B$ is taken from the d_1 computation. GOTO step 9. ELSE IF $d_2 \leq f_c$ and $\xi_n^{B(\alpha)} <$ TOL, then the step is elastic with an incorrect active set B. Set

$$\boldsymbol{\xi} = \boldsymbol{\xi}_n \tag{93}$$
$$\gamma^{B(\alpha)} = \gamma_B^\alpha , \tag{94}$$

where $\boldsymbol{\gamma}_B$ is taken from the d_2 computation. GOTO step 9. ELSE GOTO step 6.

6. **Initialize evolution computation:** Set

$$\gamma^{B(\alpha)} = \gamma_B^\alpha \qquad \text{(using } \boldsymbol{\gamma}_B \text{ from the } d_1 \text{ computation)} \tag{95}$$

$$\boldsymbol{f} = -\boldsymbol{s} + \mathcal{P}^*[\boldsymbol{\gamma}] \tag{96}$$

$$\Delta\lambda = \frac{d_1}{\|\partial^2_{\boldsymbol{f}\boldsymbol{f}} \Psi^M(\boldsymbol{\xi}_n)\partial_{\boldsymbol{f}}\phi(\boldsymbol{f})\|} \tag{97}$$

$$\delta = \frac{1}{n}\boldsymbol{e}^* \cdot [-\boldsymbol{\psi}(\boldsymbol{\varepsilon}) - \partial_{\boldsymbol{\xi}}\Psi^M(\boldsymbol{\xi}_n + \Delta\lambda\partial_{\boldsymbol{f}}\phi) + \boldsymbol{\gamma}] \tag{98}$$

Using Eqs. (52) – (55), compute the initial residual associated with the $n + m + 2$ discrete evolution equations and assemble them in the vector $\boldsymbol{R}$. Let $\text{TOL}_R = \text{TOL} \times \|\boldsymbol{R}\|$. GOTO step 7.

7. **Newton Iteration:** Using Eq. (56) compute a newton search direction as $d\boldsymbol{X} = -\boldsymbol{K}^{-1}\boldsymbol{R}$. Compute the residual associated with $\boldsymbol{X} + d\boldsymbol{X}$. IF the norm of the new residual is greater than one-half of the previous residual, then perform a line search. GOTO step 8.

8. **Newton Check:** IF $\|\boldsymbol{R}\| \leq \text{TOL}_R$, then the iteration is converged; GOTO step 9. ELSE IF $\Delta\lambda < 0$, then reset $\Delta\lambda = \text{TOL}$; then GOTO step 7.

9. **Check validity of active constraint set B:** IF $\boldsymbol{\gamma} \geq -\text{TOL}$ and $\boldsymbol{\xi} \geq -\text{TOL}$, then B is valid and the constitution is converged; STOP. ELSE CONTINUE.

10. **Correct active constraint set B:** First remove un-needed constraints.

$$B = B \setminus \{\alpha \mid \gamma^\alpha < -\text{TOL}\}\,. \tag{99}$$

Second add constraints for phase fractions that have gone negative.

$$\xi_{min} = \min_\beta \xi^\beta \tag{100}$$

$$\text{IF } \xi_{min} < -\text{TOL}, \text{ then } B = B \cup \{\alpha \mid \xi^\alpha = \xi_{min}\} \tag{101}$$

GOTO step 7.